

# ISAC: Training-Free Instance-to-Semantic Attention Control for Improving Multi-Instance Generation

**Sanghyun Jo** \*

SHJO.APRIL@GMAIL.COM

*OGQ*

*Seoul, South Korea*

**Wooyeol Lee** \*

WOoyeol0519@SNU.AC.KR

*Department of Computer Science and Engineering*

*Seoul National University*

*Seoul, South Korea*

**Ziseok Lee** \*

ZISEOKLEE@SNU.AC.KR

*Department of Biomedical Sciences*

*Seoul National University*

*Seoul, South Korea*

**Kyungsu Kim** †

KYSKIM@SNU.AC.KR

*School of Transdisciplinary Innovations and Interdisciplinary Program in Artificial Intelligence*

*Seoul National University*

*Seoul, South Korea*

## Abstract

Text-to-image diffusion models excel at generating single-instance scenes but struggle with multi-instance scenarios, often merging or omitting objects. Unlike previous training-free approaches that rely solely on semantic-level guidance without addressing instance individuation, our training-free method, **Instance-to-Semantic Attention Control (ISAC)**, explicitly resolves incomplete instance formation and semantic entanglement through an instance-first modeling approach. This enables ISAC to effectively leverage a hierarchical, tree-structured prompt mechanism, disentangling multiple object instances and individually aligning them with their corresponding semantic labels. Without employing any external models, ISAC achieves up to 52% average multi-class accuracy and 83% average multi-instance accuracy by effectively forming disentangled instances. The code will be made available upon publication.

**Keywords:** text-to-image generation, attention control, multi-instance generation, training-free, diffusion model

## 1 Introduction

Text-to-image (T2I) diffusion models [1–5] have demonstrated remarkable capabilities in generating high-quality images from textual descriptions. While these models excel at generating single objects, they often struggle when asked to create images with multiple distinct objects. For example, when prompted with “A photo of two cats and a dog”, even advanced models like SDXL [2] and SD3.5-M [3] frequently fail in two common ways, as

---

\*. Equal Contribution

†. Corresponding Author

shown in Figure 1: (1) *instance missing*, where not all requested objects appear in the image, and (2) *instance merging*, where different objects’ features blend together into a single entity.

Previous research has shown that cross-attention maps within the model’s UNet play a key role in determining object placement [6]. Based on this insight, several researchers have developed methods to manipulate these cross-attention maps [7–12]. Some methods boost attention to neglected words [9, 11], while others try to separate attention maps for different objects [10, 12, 13].

However, these approaches still struggle because they focus only on semantic features without properly understanding object shapes and boundaries. Our investigations show that even when strictly enforcing separation between attention maps using maximum pixel-wise overlap (MPO) loss (6), the results often include fragmented or unnaturally divided objects. As Figure 7 illustrates, this occurs because cross-attention maps primarily capture what objects are (semantics) but not their physical shapes and boundaries.

In this paper, we introduce **Instance-to-Semantic Attention Control (ISAC)**. While existing methods focus solely on semantic-level guidance without first resolving instance formation, ISAC explicitly addresses incomplete instance formation and multi-semantic entanglement through an instance-first generation approach.

Our key insight is that self-attention maps within the diffusion model, especially in early generation steps, naturally distinguish between different object shapes. ISAC leverages this by first establishing distinct object instances using self-attention maps, and then guiding semantic assignment through cross-attention maps. This two-phase approach enables our framework to support a hierarchical, tree-structured prompt mechanism, where multiple object instances are first disentangled and then individually aligned with their corresponding semantics.

In summary, our main contributions are:

- We identify that prior methods fail by focusing on semantic guidance without first resolving instance individuation, and propose a solution that explicitly models instance formation before semantic assignment.
- ISAC introduces a hierarchical, tree-structured approach that first disentangles object instances using self-attention maps, then aligns each instance with its corresponding semantics through instance-aware semantic attention.
- Our method significantly outperforms existing approaches across multiple model architectures (SD1.5 [1], SDXL [2], SD3.5-M [3]), achieving up to 52% average multi-class accuracy and 83% average multi-instance accuracy by effectively forming disentangled instances.

## 2 Related Work

**Cross-Attention Manipulation for Semantic Control.** The pivotal work of [6] established cross-attention maps as the primary interface between text semantics and spatial layouts in diffusion models. This insight spawned two dominant strategies for multi-instance generation: *attention enhancement* [7–9, 11] and *attention separation* [10, 12–14]. Attend-and-Excite [9] pioneered the former approach by maximizing attention response peaks for



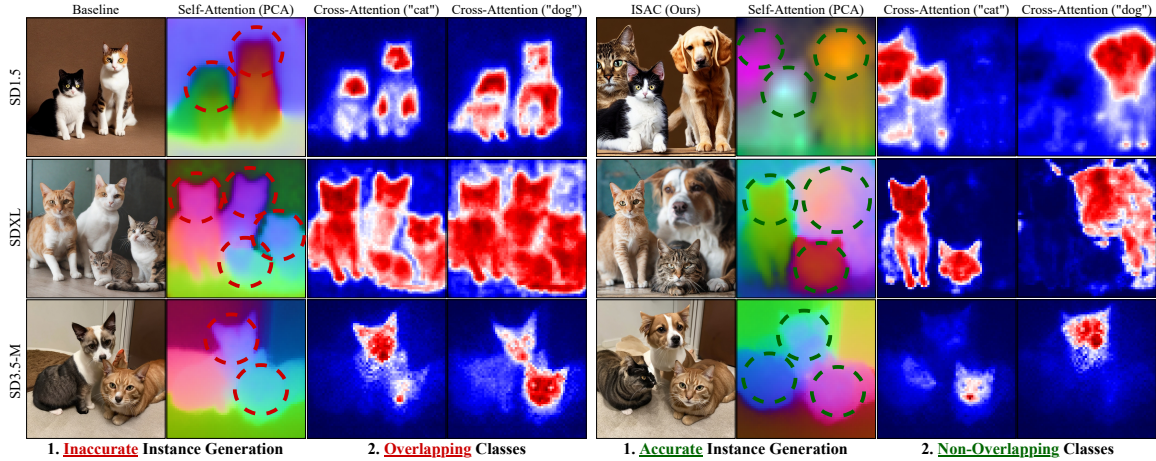


Figure 1: Comparison between existing text-to-image diffusion models [1–3] (left) and the proposed ISAC framework (right) on the prompt "A photo of two cats and a dog". Current methods (SD1.5 [1], SDXL [2], SD3.5-M [3]) struggle to clearly separate individual instances, leading to merged or overlapped objects (red dashed circles). In contrast, our ISAC explicitly utilizes early-stage self-attention to accurately identify distinct, non-overlapping instances (green dashed circles) and assigns them precise semantic labels, resulting in clear class boundaries without additional training or supervision.

neglected objects, this often creates overlapping regions that lead to instance merging. Subsequent methods like InitNO [11] introduced noise optimization to strengthen cross-attention signals but remained constrained by their focus on localized features rather than holistic shapes. TEBOpt [8] shows interesting perspective by optimizing CLIP [15] text embeddings via strengthening single instance embedding signals. The separation paradigm, exemplified by SynGen [10], employs syntactic analysis and KL-divergence losses to minimize overlap between unrelated entities’ attention maps. However, our experiments in Figure 7 and Table 3 reveal these global distribution metrics, such as KL-divergence and Intersection-of-Union (IoU), fail to enforce the pixel-level discontinuities needed for distinct instances.

**Self-Attention for Structural Guidance.** While most methods focus on cross-attention, recent work hints at self-attention’s untapped potential. Particularly relevant to multi-instance scenarios, [16] observed that early-step self-attention maps excel at decoupling distinct instance shapes, while cross-attention maps maintain a primary focus on semantic features throughout various stages. InitNO [11] briefly explores self-attention peaks but lacks ISAC’s systematic framework for converting these signals into coherent instance masks. Figure 2 illustrates this observation, showing that self-attention maps in early diffusion steps effectively delineate distinct instance shapes, finalizing the instance layout then the capability diminishes in later steps. It is also noteworthy that some approaches, such as [17, 18], propose using pretrained vision models to enhance multi-instance generation. However, these models, such as Grounding DINO [19], often struggle in the early diffusion steps where semantic information is still nascent, highlighting the strength of ISAC’s intrinsic signal.

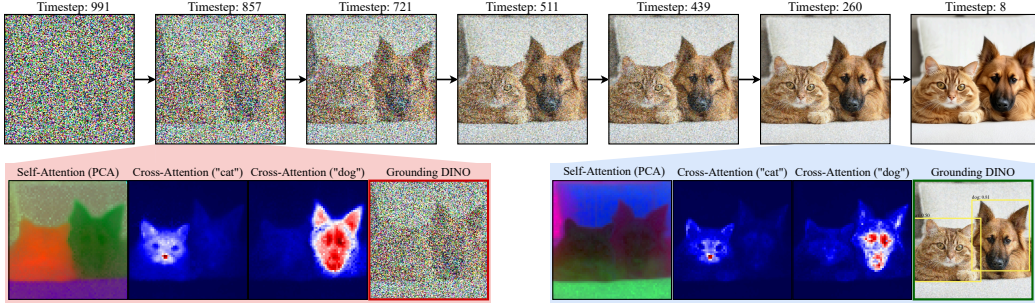


Figure 2: Instance-to-semantic dynamics in diffusion models. Early diffusion steps prioritize instance decoupling, where self-attention maps begin to delineate distinct shapes, while later steps refine semantic details. The figure also illustrates that semantic features of denoised image are nascent in early stages, making guidance from pretrained vision models such as Grounding DINO [19] challenging until semantics become clearer. We used SD3.5-M [3] for visualization.

**Decoupling Instance and Semantic Refinement.** The dichotomy between structural formation and semantic assignment mirrors findings in diffusion process analysis. [20] established through Fourier analysis that low-frequency structural components emerge early, while high-frequency details develop later. ISAC operationalizes this insight by aligning self-attention guidance in early diffusion steps and cross-attention refinement in later diffusion steps, avoiding the conflicting objectives that plague single-stage approaches.

### 3 Preliminaries

We consider the text-to-image generation task, where a text prompt  $C$  is given as input to a latent diffusion model to generate a corresponding image. We focus on prompts where  $C$  contains one or more object categories (e.g., "cat", "dog", "car"). From  $C$ , we assume access to a set of class tokens  $\tau_1, \dots, \tau_k$  and their respective instance counts  $n_1, \dots, n_k$ .

#### 3.1 Latent Diffusion Models

Diffusion models define a forward noising process and a learned reverse denoising process. Let  $X_0 \sim p_0$  be a sample from the target data distribution, and let  $X_T \sim p_T$  be a fully noised sample. The forward process gradually corrupts  $X_0$  into  $X_T$  through a sequence of intermediate latents  $X_1, \dots, X_T$  by applying Gaussian noise. A neural network  $\epsilon_\theta(X_t, t, \mathcal{T})$  is trained to predict the noise component  $\epsilon$ , conditioned on timestep  $t$  and the text embedding  $\mathcal{T} \in \mathbb{R}^{L \times d}$ , where  $L$  is the number of text tokens (including class tokens  $\tau_1, \dots, \tau_k$ ) and  $d$  is the embedding dimension. The network is optimized via:

$$\theta^* = \operatorname{argmin}_{\theta \in \Theta} \mathbb{E}_{(X_0, \mathcal{T}), \epsilon, t} [\|\epsilon_\theta(X_t, t, \mathcal{T}) - \epsilon\|_2^2]$$

**Sample Generation.** The model defines a trajectory  $X_T \rightarrow X_{T-1} \rightarrow \dots \rightarrow X_0$ , gradually refining an initial random noise  $X_T \sim \mathcal{N}(0, I)$  into a clean image latent  $X_0$ , conditioned on prompt embedding,  $\mathcal{T}$ . The specific form of the update rule depends on

the generative modeling framework. We use  $X_{t-1} \leftarrow \text{Denoise}(X_t, \epsilon_\theta, t)$  to denote a single denoising step. In DDPMs [21], the model computes the posterior  $p_\theta(X_{t-1} | X_t)$  to obtain  $X_{t-1}$ . In ODE-based methods like Flow Matching [3], the model predicts the instantaneous velocity field  $v_\theta(X_t, t, \mathcal{T})$  and the denoising step is taken by  $X_{t-dt} = X_t - dt \cdot v_\theta(X_t, t, \mathcal{T})$ . Our framework is agnostic to the specific generative dynamics; it only requires access to the latent  $X_t$  at each timestep  $t$  and the attention layers.

**Architecture.** The model  $\epsilon_\theta$  (or  $v_\theta$ ) consists of an image encoder  $\mathcal{E}$ , a decoder  $\mathcal{D}$ , and multiple U-Net/DiT transformer blocks with self- and cross-attention layers. Given an image  $I$ , its latent representation is  $X_0 = \mathcal{E}(I)$ , and training/generation proceeds in latent space. After denoising, the latent is decoded back to image space via  $\hat{I} = \mathcal{D}(\hat{X}_0)$ . The model  $\epsilon_\theta$  (or  $v_\theta$ ) uses attention mechanisms to relate spatial features and align them with text. Let  $X_t \in \mathbb{R}^{H \times W \times d}$  be the latent at timestep  $t$ , reshaped to  $\mathbb{R}^{HW \times d}$ . The transformer blocks compute self-attention which capture dependencies between spatial locations within the latent image and cross-attention which aligns each spatial location in the latent with text tokens.

**Self-Attention.** For a given head, weights  $W_Q^{\text{self}} \in \mathbb{R}^{d \times d_h}$  and  $W_K^{\text{self}} \in \mathbb{R}^{d \times d_h}$  are learned. The self-attention maps are computed as  $Q_t^{\text{self}} = X_t W_Q^{\text{self}}$ ,  $K_t^{\text{self}} = X_t W_K^{\text{self}}$ ,  $Q_t, K_t \in \mathbb{R}^{HW \times d_h}$ :

$$SA(X_t) = \text{softmax} \left( Q_t^{\text{self}} K_t^{\text{self}^\top} / \sqrt{d_h} \right) \in [0, 1]^{HW \times HW} \quad (1)$$

**Cross-Attention.** Let  $\mathcal{T} \in \mathbb{R}^{L \times d}$  be the text embedding of prompt  $C$  (including class tokens). After learning the weights  $W_Q^{\text{cross}}, W_K^{\text{cross}} \in \mathbb{R}^{d \times d_h}$ , the cross-attention maps are computed as  $Q_t^{\text{cross}} = X_t W_Q^{\text{cross}}$ ,  $K_t^{\text{cross}} = \mathcal{T} W_K^{\text{cross}}$ ,  $Q_t \in \mathbb{R}^{HW \times d_h}$ ,  $K_t \in \mathbb{R}^{L \times d_h}$ :

$$CA(X_t, \mathcal{T}) = \text{softmax} \left( Q_t^{\text{cross}} K_t^{\text{cross}^\top} / \sqrt{d_h} \right) \in [0, 1]^{HW \times L} \quad (2)$$

**Attention Accumulation and Hook Function.** Most models have multiple transformer layers with varying resolutions. To access intermediate attention maps during inference, we implement hook functions,  $\mathcal{H}^{\text{self}}, \mathcal{H}^{\text{cross}}$ , which attach to self- and cross-attention layers in  $\epsilon_\theta$  (or  $v_\theta$ ) without altering the forward computation.  $\mathcal{H}^{\text{self}}, \mathcal{H}^{\text{cross}}$  each return a single accumulated self-/cross-attention map.

Let there be  $M$  attention layers (at spatial resolutions  $H_l \times W_l$ ) and  $h_l$  attention heads at the  $l$ -th layer. Each head in each layer produces a self-attention map  $SA_l^h \in \mathbb{R}^{H_l W_l \times H_l W_l}$  or cross-attention map  $CA_l^h \in \mathbb{R}^{H_l W_l \times L}$ . We upsample each  $SA_l^h$  and  $CA_l^h$  to the highest spatial resolution  $H \times W$ , and accumulate them by averaging across all heads and all resolutions:

$$\mathcal{H}^{\text{self}}(X_t, \mathcal{T}, \epsilon_\theta, t) = \frac{1}{\sum_{l=1}^M h_l} \sum_{l=1}^M \sum_{h=1}^{h_l} \text{Upsample}(SA_l^h, \delta_l) \in \mathbb{R}^{HW \times HW} \quad (3)$$

$$\mathcal{H}^{\text{cross}}(X_t, \mathcal{T}, \epsilon_\theta, t) = \frac{1}{\sum_{l=1}^M h_l} \sum_{l=1}^M \sum_{h=1}^{h_l} \text{Upsample}(CA_l^h, \delta_l) \in \mathbb{R}^{HW \times L} \quad (4)$$

where  $\delta_l = H/H_l = W/W_l$  is the upsampling factor for the  $l$ -th layer.

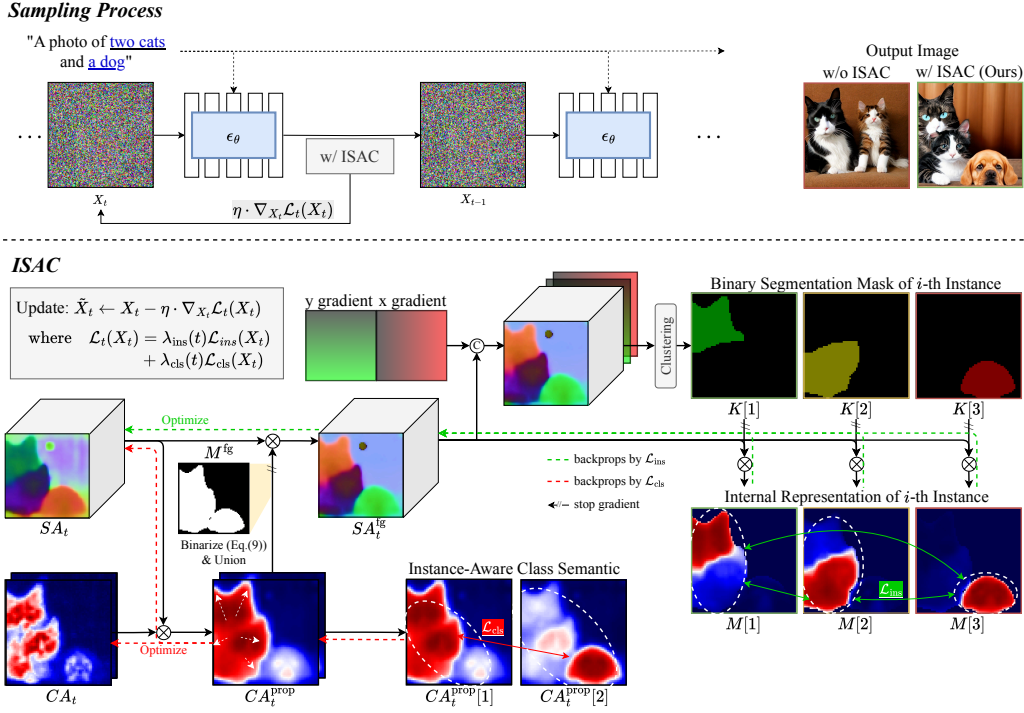


Figure 3: Overview of ISAC optimization process. At each denoising step, we update the latent by  $\mathcal{L}_{ins}$  and  $\mathcal{L}_{cls}$  losses.  $\mathcal{L}_{ins}$  is first applied to encourage self-attention maps to form correct number of instances. Then, with the optimized instance structure,  $\mathcal{L}_{ins}$  ensures each class semantic corresponds to the most probable instances.

## 4 Method

We propose ISAC, a latent optimization framework that optimizes  $X_t$  directly using the accumulated attention maps from  $\mathcal{H}^{self}$ ,  $\mathcal{H}^{cross}$  to achieve instance individuation and precise class assignment. We first present the high-level objective before detailing the components in Sections 4.1 and 4.2. ISAC optimizes a time-dependent loss (5).

$$\mathcal{L}_t(X_t) := \lambda_{ins}(t) \mathcal{L}_{ins}(X_t) + \lambda_{cls}(t) \mathcal{L}_{cls}(X_t) \quad (5)$$

The first term,  $\mathcal{L}_{ins}$  enforces *instance decoupling* to distinguish individual instance regions within the generated image (Section 4.1). The second term,  $\mathcal{L}_{cls}$  ensures *class disambiguation* with instance guidance, accurately associating each decoupled instance with a single corresponding class label to prevent mixed classes within a single instance (Section 4.2). The time-dependent coefficients  $\lambda_{ins}(t)$ ,  $\lambda_{cls}(t)$  dynamically adjust the balance, emphasizing instance decoupling during the early stages (when instance composition can be effectively controlled) and switching towards class separation during the later stages (when instance composition is finalized but class details can change). This is motivated by the observed dynamics of instance formation in Figure 2. We provide a visual overview in Figure 3 and the optimization algorithm of the ISAC framework in Algorithm 1.

---

**Algorithm 1:** Latent Optimization by ISAC

---

**Input:** Prompt  $\mathcal{T}$ , Model  $\epsilon_\theta$ , decoder  $\mathcal{D}$ , Learning rate  $\eta$   
**Output:** Image  $I_0$  with decoupled instances and class separation

```
1  $X_T \sim \mathcal{N}(0, I)$  // Sample initial noise
2 for  $t = T, T-1, \dots, 1$  do
3   Call Denoise( $X_t, \epsilon_\theta, t$ ) with Hook functions  $\mathcal{H}^{\text{self}}, \mathcal{H}^{\text{cross}}$ 
4    $SA_t \leftarrow \mathcal{H}^{\text{self}}(X_t, \mathcal{T}, \epsilon_\theta, t)$ 
5    $CA_t \leftarrow \mathcal{H}^{\text{cross}}(X_t, \mathcal{T}, \epsilon_\theta, t)$ 
6    $CA_t^{\text{prop}} \leftarrow SA_t \cdot CA_t$  // Propagation
7   Compute  $\mathcal{L}_{\text{ins}}, \mathcal{L}_{\text{cls}} \leftarrow (8), (9), (11), (12)$ 
8    $\mathcal{L}_t(X_t) \leftarrow \lambda_{\text{ins}}(t)\mathcal{L}_{\text{ins}}(X_t) + \lambda_{\text{cls}}(t)\mathcal{L}_{\text{cls}}(X_t)$ 
9   Latent optimization:  $\tilde{X}_t \leftarrow X_t - \eta \cdot \nabla_{X_t} \mathcal{L}_t(X_t)$ 
10   $X_{t-1} \leftarrow \text{Denoise}(\tilde{X}_t, \epsilon_\theta, t)$ 
11  $I_0 \leftarrow \mathcal{D}(X_0)$  // Decode to pixel space
```

---

**MPO.** At the core of our loss function, we introduce a novel local similarity metric, the *Maximum Pixel-wise Overlap (MPO)*, tailored for soft masks. Unlike global similarity metrics such as IoU or KL divergence, MPO directly penalizes the peak spatial co-activation between two continuous masks, encouraging spatial exclusivity between them. Formally, let  $A, B \in [0, 1]^F$  denote soft masks over the spatial domain of  $F$  pixels. We define the *maximum pixel-wise overlap* as:

$$\text{MPO}(A, B) = \max_{p \in \{1, \dots, F\}} (A[p] \cdot B[p]) \quad (6)$$

MPO captures the worst-case conflict between regions—penalizing even small overlaps if they are sharply localized. This makes it effective for instance decoupling and class disambiguation, where distinct instances or classes should not share spatial regions, even partially. Soft masks derived from attention maps often exhibit ambiguous boundaries, and MPO ensures that the learned instance masks become more exclusive and spatially separated during training. We provide a thorough comparison and ablation of these design choices in Section 5.3 and Figure 7.

**Class Propagation.** Let  $CA_t \in [0, 1]^{HW \times L}$ ,  $SA_t \in [0, 1]^{HW \times HW}$  denote the accumulated cross- and self-attention map at timestep  $t$ , respectively, where  $L$  is the length of the prompt token sequence. We expect  $SA_t$  to have fully decoupled instances after optimizing (8). Thus, we use  $SA_t$  to propagate the cross-attention map  $CA_t$  throughout the region of the corresponding token, denoted by:

$$CA_t^{\text{prop}}(X_t, \mathcal{T}) \leftarrow SA_t \cdot CA_t \in [0, 1]^{HW \times L} \quad (7)$$

Class propagation is commonly used in segmentation [22–25]. We follow [22] and propagate the cross-attention map  $CA_t$  by multiplying it with the corresponding self-attention map  $SA_t$  as in (7). The reason for this computation lies in the ability of self-attention maps to estimate the correlation between pixels, allowing cross-attention to compensate for incomplete activation regions and perform region completion (see Figure 4).

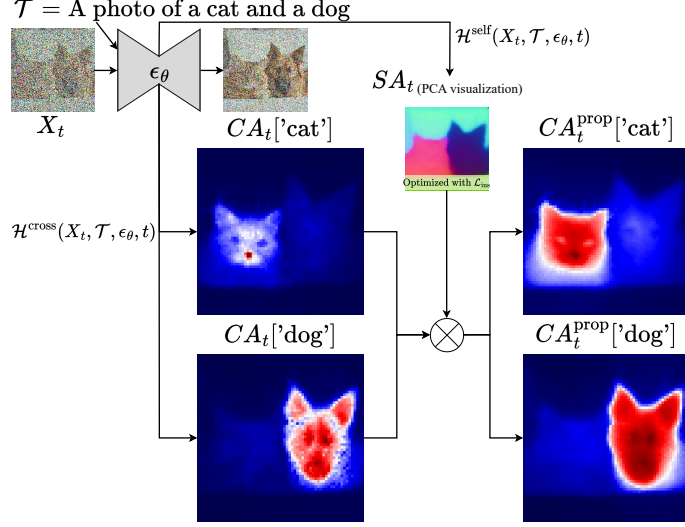


Figure 4: Self-attention-based class propagation is a simple way to propagate local class information within instances while preventing class mixing.

#### 4.1 Instance Decoupling

The first loss term  $\mathcal{L}_{\text{ins}}(X_t)$  enforces instance individuation by penalizing the overlap between distinct instance regions. Suppose we have  $k$  classes, represented by class tokens  $\tau_1, \dots, \tau_k$  and a total of  $N = n_1 + \dots + n_k$  instances. Since we know the total number of instances, we can apply K-means clustering to the foreground region of the self-attention map and obtain soft masks  $M[i] \in [0, 1]^{HW}$  representing individual instances, where  $i = 1, \dots, N$ . The loss is designed to penalize the maximum pixel-wise overlap (6) between soft masks of distinct instances, defined as:

$$\mathcal{L}_{\text{ins}}(X_t) = \max_{1 \leq i < j \leq N} \text{MPO}(M[i], M[j]) \quad (8)$$

**Details on obtaining  $M[i]$ .** Suppose that the denoising timestep is  $t$ . In order to cluster the instances properly, we need to first mask the foreground (i.e., the union of all instances) such that the background does not interfere with the clustering. Following [26], we create a *global foreground mask* using the propagated cross-attention map  $CA_t^{\text{prop}} \in [0, 1]^{HW \times L}$  from (7). Using the column-wise mean,  $\mu_j$ , as an adaptive threshold, we convert  $CA_t^{\text{prop}}$  to a binary mask via  $CA_t^{\text{bin}} \leftarrow \text{Binarize}(CA_t^{\text{prop}})$ :

$$\text{Binarize}(CA_t^{\text{prop}})[i, j] = \mathbf{1}[CA_t^{\text{prop}}[i, j] > \mu_j] \in \{0, 1\} \quad (9)$$

The binarized map  $CA_t^{\text{bin}} \in \{0, 1\}^{HW \times L}$  contains foreground masks for each class token  $\tau_1, \dots, \tau_k$  (e.g., "dog", "cat") as well as non-class tokens (e.g., "the", "and"). The *global foreground mask*  $M_{\text{fg}}$  is the union of the masks corresponding to class tokens:  $M_{\text{fg}} = \bigcup_{\tau[i] \in \{\tau_j\}_{j=1}^k} CA_t^{\text{bin}}[:, i] \in \{0, 1\}^{HW}$ .



We take the index set  $\mathcal{I}$  of nonzero elements of  $M_{\text{fg}}$  to obtain the *filtered self-attention map*  $SA_t^{\text{fg}}$ :

$$\mathcal{I} = \{i : M_{\text{fg}}[i] = 1\}, \quad SA_t \leftarrow \mathcal{H}^{\text{self}}(X_t, \epsilon_\theta, t) \quad (10)$$

$$SA_t^{\text{fg}} \leftarrow SA_t[\mathcal{I}, \mathcal{I}] \in [0, 1]^{F \times F}, \text{ where } F := |\mathcal{I}| \quad (11)$$

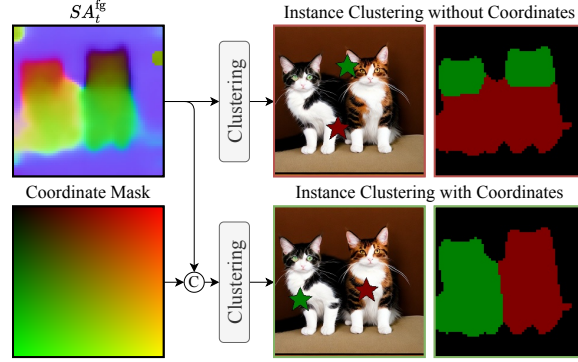


Figure 5: Adding X/Y coordinate masks improves instance clustering by introducing spatial cues, avoiding incorrect merging of separate instances.

For robust clustering, we add X/Y coordinate masks as in Figure 5, obtaining a final  $F \times (F + 2)$ -dimensional tensor. Viewing this tensor as a collection of  $F$ -many  $(F + 2)$ -dimensional vectors, we simply use the K-means clustering algorithm with  $K = N$  to obtain  $N$  clusters among  $F$  data points. This is represented as a one-hot encoded matrix  $K \in \{0, 1\}^{F \times N}$ . We refer to  $K$  as the *hard binary instance mask*.

Finally, we take the matrix product  $SA_t^{\text{fg}} \cdot K \in [0, 1]^{F \times N}$  and denote the column vectors as  $M[1], M[2], \dots, M[N] \in [0, 1]^F$ . Since  $SA_t^{\text{fg}}$  is a masked self-attention map, its  $p$ -th column is a spatial dependency map of the  $p$ -th pixel with every other pixel in the foreground (close to 1 if the pixels are part of the same instance and close to 0 if the pixels are unrelated). Taking the matrix product with  $K$ ,  $M[i]$  is the sum of all dependency maps of pixels in the  $i$ -th instance. Hence,  $M[i]$  can be interpreted as an internal representation of the  $i$ -th instance. Problematic cases arise when internal representations of different instances  $i \neq j$ , intersect each other  $M[i] \cap M[j] \neq \emptyset$ , leading to missing/mixed instances. We penalize this by minimizing the MPO between  $M[i], M[j]$  for all  $i \neq j$ , as formulated in (8).

## 4.2 Instance-Guided Class Disambiguation

Decoupling instances is not enough; each instance should be assigned a *single, unambiguous* class. Ambiguous class assignments result in semantically inconsistent generation results (e.g., a dog’s head on a horse’s body). To decouple class assignments, we formulate  $\mathcal{L}_{\text{cls}}(X_t)$ . We take the propagated cross-attention map  $CA_t^{\text{prop}}$  from (7) and discard columns corresponding to non-class tokens. This yields the filtered cross-attention map  $CA_t^{\text{cls}} \in [0, 1]^{HW \times k}$  where  $k$  is the number of classes. Each column of  $CA_t^{\text{cls}}$  represents the spatial support (i.e., soft mask) of a single class. We penalize the maximum pixel-wise overlap (6) between the soft

masks of distinct classes, defined as:

$$\mathcal{L}_{\text{cls}}(X_t) = \max_{1 \leq i < j \leq k} \text{MPO}(CA_t^{\text{cls}}[i], CA_t^{\text{cls}}[j]) \quad (12)$$

Minimizing (12) can be interpreted as pushing cross-attention toward the correct region and away from incorrect ones when a class token activates multiple regions, separating mixed classes.

## 5 Experiments

### 5.1 Experimental Setup

**Evaluation Metrics.** To assess the performance of our method, we define two tasks: multi-class generation and multi-instance generation. Multi-class generation requires generating multiple classes with a single instance for each class, while multi-instance generation requires generating multiple instances for a single class. Unlike multi-class generation, where each class tag can serve as an auxiliary signal for the corresponding instance, multi-instance generation task requires a more complex approach to ensure that multiple instances are generated for a single class.

We evaluate the performance of our method using the following metrics:

- **Multi-class accuracy (%)**: The percentage of classes that are generated correctly, where a class is considered correct if the generated instance matches the target class.
- **Multi-instance accuracy (%)**: The percentage of instances that are generated correctly, where an instance is considered correct if it matches the target class and is spatially separated from other instances.

**Implementation Details.** For fair comparison, we follow the official settings (CFG and sampling steps) reported in each paper for SD1.5 [1], SDXL [2], and SD3.5-M [3]. All class tags in the evaluation prompts are taken from COCO [27] classes; see the Appendix for prompt formatting details. For **Multi-class accuracy**, we construct all non-overlapping class pairs from the given set and report the average accuracy across these combinations. To evaluate generation accuracy, we adopt the widely used Grounding DINO [19] and further ensemble it with YOLOv12 [28] and YOLOE [29] to reduce single-model errors; details of the ensemble process are in the Appendix. All experiments are conducted on a single A100 GPU (80GB). In Algorithm 1, the only tunable hyperparameter is the learning rate  $\eta$ , which is fixed to 0.01 across all text-to-image diffusion models. Related ablation studies are included in the Appendix.

### 5.2 Main Results

**ISAC Significantly Improves Multi-Class and Multi-Instance Generation Performance.** Table 1 quantitatively compares ISAC with several baselines across three backbone diffusion models (SD2.1 [1], SDXL [2], and SD3.5-M [3]) on multi-class and multi-instance generation tasks. ISAC consistently achieves the highest average multi-class and multi-instance accuracy across all settings.



Table 1: Quantitative comparison of ISAC (Ours) and baseline methods on multi-class and multi-instance generation (2–5 classes, 2–5 instances). ISAC consistently achieves the highest performance across all models while maintaining comparable latency and VRAM usage to baseline methods.

Method	Multi-Class Accuracy ( $\uparrow$ )					Multi-Instance Accuracy ( $\uparrow$ )					Latency ( $\downarrow$ )	VRAM ( $\downarrow$ )
	#2	#3	#4	#5	Average	#2	#3	#4	#5	Average		
SD1.5 [1]	28%	2%	1%	0%	8%	88%	65%	36%	26%	54%	<b>12s</b>	<b>4.4GB</b>
+ A&E [9]	48%	10%	5%	2%	16%	91%	68%	34%	24%	54%	24s	9.1GB
+ SynGen [10]	50%	9%	4%	2%	16%	84%	61%	38%	22%	51%	27s	9.2GB
+ InitNO [11]	55%	12%	7%	5%	20%	90%	68%	40%	29%	57%	29s	9.5GB
+ TEBOpt [8]	52%	11%	8%	3%	18%	87%	65%	36%	27%	54%	25s	9.2GB
<b>+ ISAC (Ours)</b>	<b>65%</b>	<b>31%</b>	<b>29%</b>	<b>18%</b>	<b>36%</b>	<b>95%</b>	<b>82%</b>	<b>56%</b>	<b>44%</b>	<b>69%</b>	30s	9.6GB
SDXL [2]	20%	4%	3%	0%	7%	90%	71%	49%	32%	61%	<b>48s</b>	<b>12.8GB</b>
<b>+ ISAC (Ours)</b>	<b>57%</b>	<b>32%</b>	<b>29%</b>	<b>17%</b>	<b>34%</b>	<b>96%</b>	<b>89%</b>	<b>71%</b>	<b>47%</b>	<b>76%</b>	101s	29.8GB
SD3.5-M [3]	62%	23%	12%	3%	25%	84%	71%	51%	51%	64%	<b>40s</b>	<b>22.9GB</b>
<b>+ ISAC (Ours)</b>	<b>98%</b>	<b>51%</b>	<b>40%</b>	<b>20%</b>	<b>52%</b>	<b>98%</b>	<b>91%</b>	<b>72%</b>	<b>69%</b>	<b>83%</b>	140s	74.8GB

**Multi-Class Accuracy.** ISAC demonstrates strong improvements across all numbers of target classes. When integrated with SD1.5, ISAC improves the average multi-class accuracy from 8% to 36%, outperforming all other baselines by a large margin. Similar gains are observed with SDXL (from 7% to 34%) and SD3.5-M (from 25% to 52%).

**Multi-Instance Accuracy.** ISAC also boosts the model’s ability to handle multiple instances of the same class. On SD1.5, ISAC increases the average accuracy from 54% to 69%, and on SD3.5-M, from 64% to 83%, reflecting ISAC’s effectiveness at enforcing instance-aware control during generation.

**Scalability and Versatility Across Backbones.** Notably, ISAC scales across different model sizes and capabilities. Even though SDXL and SD3.5-M are substantially more capable and larger than SD1.5, ISAC consistently improves both class and instance metrics across the board, indicating that its gains are architecture-agnostic.

**Qualitative Results.** Figure 6 shows that in most cases SD1.5 [1], A&E [9], InitNO [11] (1st, 3rd rows) and SynGen [10] (1st, 2nd row) fail to generate all 3 instances. Even succeed in generating 3 instances, they often wrongly allocate the class labels—A&E [9] and InitNO [11] (2nd row) and SynGen [10] (3rd row)—leading to another instance missing problem. Also in the case of SD1.5 [1], A&E [9] and InitNO [11] (2nd row), the left dog with brown hair indicates semantic features from adjacent instances flooded to it, which is a common failure mode of instance merging. In contrast, ISAC successfully generates 3 decoupled instances with distinct appearances, demonstrating its effectiveness in multi-instance generation.

### 5.3 Ablation Study

**Contribution of Loss Components.** To assess the contribution of the instance decoupling loss  $\mathcal{L}_{\text{ins}}$  and class disambiguation loss  $\mathcal{L}_{\text{cls}}$ , we perform an ablation study by selectively removing each component and analyzing the resulting changes in multi-class and multi-instance accuracy. As shown in Table 2, both loss terms are essential for achieving balanced performance across both metrics. Comparing configurations (A), (B), and (C), we find that



Figure 6: Qualitative comparison among various attention control methods. For all cases, we provide “A photo of two cats and a dog” as an input prompt and use SD1.5 [1] as a baseline diffusion model.

Table 2: Different weights  $\lambda_{\text{ins}}(t)$ ,  $\lambda_{\text{cls}}(t)$  and their multi-class/multi-instance accuracy. Here, we use  $\lambda_{\text{cls}}(t) = 1 - \lambda_{\text{ins}}(t)$  for the purpose of balancing the two components in (5), SD1.5 [1] is the backbone diffusion model.

Config.	Description	$\lambda_{\text{ins}}(t)$	$\lambda_{\text{cls}}(t)$	Multi-Class Accuracy	Multi-Instance Accuracy
A	Only Instance Optimization	1	0	10% (-26%pt)	65% (-4 %pt)
B	Only Class Optimization	0	1	28% (-8 %pt)	54% (-15%pt)
C	Fixed Balance	0.5	0.5	25% (-11%pt)	60% (-9 %pt)
D	Class-to-Instance	$1 - t/T$	$t/T$	21% (-15 %pt)	55% (-14%pt)
E	Instance-to-Class (Ours)	$t/T$	$1 - t/T$	<b>36%</b>	<b>69%</b>

Table 3: Alternative similarity metrics for the proposed MPO in (6). We use  $\lambda_{\text{ins}}(t) = 1 - t/T$  and  $\lambda_{\text{cls}}(t) = t/T$  for all configurations.

Loss type	Multi-Class Accuracy	Multi-Instance Accuracy
MAE	9 % (-27%pt)	55% (-14%pt)
KL	16% (-20%pt)	60% (-9%pt)
IoU	20% (-16%pt)	61% (-8%pt)
MPO (Ours)	<b>36%</b>	<b>69%</b>

optimizing only for class disambiguation (B) hurts multi-instance accuracy (-15%pt), whereas optimizing only for instance decoupling (A) degrades significantly multi-class accuracy (-26%pt). Constant weights (C) achieve a better overall balance between multi-class and multi-instance accuracy.

**Importance of Aligning Instance-to-Class Dynamics.** To validate the effectiveness of our instance-to-class scheduling strategy, we compare three weighting configurations for  $\lambda_{\text{ins}}(t)$ ,  $\lambda_{\text{cls}}(t)$ : (C) constant weights, (D) class-to-instance (linearly increasing instance weight over time), and (E) instance-to-class (our proposed schedule, with linearly decreasing instance weight). As shown in Table 2, our instance-to-class schedule (E) yields the best performance, while the reversed variant (D) performs worse than a constant baseline (C). These results highlight the importance of synchronizing optimization with the generative dynamics of the diffusion process: early steps should focus on decoupling instance masks, while later

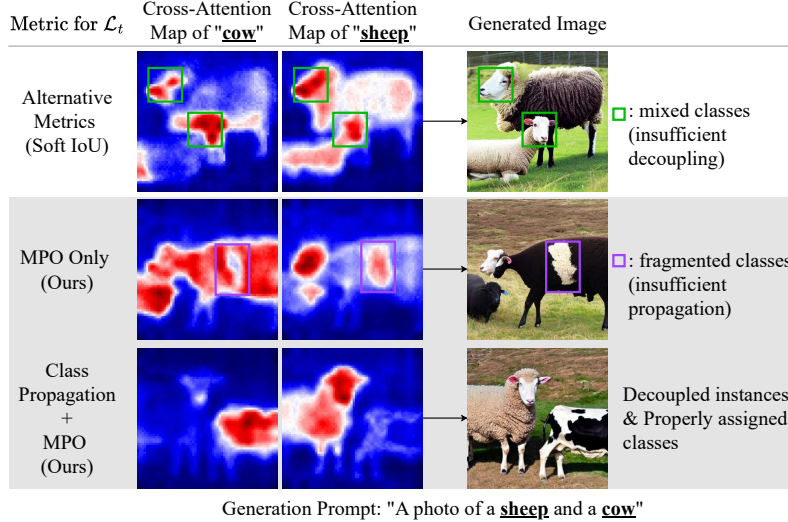


Figure 7: Effect of MPO and Class Propagation. Compared to the baseline metric, our full method produces better instance decoupling and class consistency in multi-class prompts.

steps should refine their semantic class assignments. Reversing this progression disrupts the natural structure emergence, leading to degraded performance. This aligns with our design intuition that clean spatial disentanglement must occur before meaningful semantic labeling.

### Effectiveness of Maximum Pixel-wise Overlap (MPO) and Class Propagation.

We conduct a dedicated analysis to validate the effectiveness of our proposed Maximum Pixel-wise Overlap (MPO) metric, focusing on its ability to enforce instance decoupling and class disambiguation. As shown in Table 3, MPO significantly outperforms alternative loss functions such as MAE, KL divergence, and Soft IoU in both multi-class and multi-instance accuracy. Specifically, MPO yields a 36% multi-class accuracy, which is a +16%pt gain over the best-performing baseline (IoU), and a 69% multi-instance accuracy, surpassing alternatives by up to +14%pt. These improvements highlight MPO’s ability to achieve sharper and more discriminative attention boundaries between classes and instances, which are essential for fine-grained generation control.

Figure 7 provides compelling visual evidence of MPO’s contribution. When optimized with alternative metrics such as Soft IoU, cross-attention maps exhibit significant overlap between different class regions (e.g., "cow" and "sheep"), resulting in mixed class activations and semantic leakage in the generated image (green boxes). This demonstrates that global metrics fail to enforce strict spatial exclusivity in local attention peaks. By contrast, using MPO alone leads to much clearer spatial separation between class attention maps. However, we observe some fragmented or under-propagated class activations (purple boxes), likely due to insufficient guidance in spreading class signals across instance regions. This motivates our final design that combines MPO with class propagation, effectively mitigating both overlap and fragmentation. The result is fully decoupled, semantically consistent instances, as evidenced by the sharp and well-localized attention maps and the cleanly separated classes in the final image.

## 6 Limitations

**Latency and VRAM Overhead.** While ISAC introduces an increase in latency and VRAM usage—typically around  $2\times$  to  $3.3\times$  compared to base models (see Table 1)—this overhead is a known limitation inherent to latent optimization-based methods. Importantly, the computational cost remains comparable to existing approaches like A&E, SynGen, and InitNO. Moreover, the overhead does not scale significantly with the number of target instances or classes, demonstrating ISAC’s efficiency and robustness in complex settings.

## 7 Conclusion

In this work, we address the fundamental challenge of accurately generating multiple distinct object instances in text-to-image diffusion models, specifically targeting common issues of instance merging and omission. To overcome these challenges, we propose ISAC, a novel inference-time intervention method that explicitly decouples instances using early-stage self-attention and subsequently aligns them semantically through a hierarchical, instance-first attention mechanism. Our approach significantly enhances multi-instance fidelity, demonstrating up to 52% average multi-class accuracy and 83% average multi-instance accuracy, marking a considerable improvement over existing state-of-the-art methods. This underscores the importance of instance-aware structural guidance during denoising for faithful and scalable multi-object generation, highlighting promising avenues for future exploration.

## Acknowledgments and Disclosure of Funding

Kyungsu Kim is affiliated with the School of Transdisciplinary Innovations, Department of Biomedical Science, Medical Research Center, Interdisciplinary Program in Bioengineering, and Interdisciplinary Program in Artificial Intelligence at Seoul National University, Seoul, Republic of Korea.

This work was supported by a grant of the Korea Health Technology R&D Project through the Korea Health Industry Development Institute (KHIDI), funded by the Ministry of Health & Welfare, Republic of Korea. Additionally, this research was conducted as part of the "AI Media and Cultural Enjoyment Expansion" Project, supported by the Ministry of Science and ICT and the National IT Industry Promotion Agency (NIPA) in 2025.



## Appendix

### Appendix A. Broader Impacts

Our method is designed to assist users in generating images containing multiple instances, which can be particularly beneficial for applications like synthesizing data for training machine learning models. However, there is also potential for misuse of this technology, especially in creating misleading or harmful content, such as deepfakes or other types of disinformation. These activities raise significant concerns about privacy, security, and ethical implications. Therefore, it is crucial to regulate and monitor the use of such applications and to ensure responsible utilization of the technology.

### Appendix B. Implementation Details

#### B.1 Method Details

**Choice of the Learning Rate  $\eta$ .** We conducted experiments to evaluate the sensitivity of our method to the learning rate  $\eta$  (Algorithm 1 with our time-dependent coefficients  $\lambda_{\text{ins}}(t) = 1 - t/T$  and  $\lambda_{\text{cls}}(t) = t/T$ ). When the learning rate is too low, the optimization loss does not converge, and thus has little to no effect on the outcome. Conversely, excessively high learning rates lead to latent collapse, resulting in image quality degradation. Existing studies that use latent optimization methods all share this same limitation, and our method is no exception.

We found that a learning rate of 1e-2 is sufficient for stable optimization. Additionally, we tested values in the range of 5e-3 to 1e-1 and observed consistent trends in Figure 8. We clarify that the gradient descent step  $\tilde{X}_t \leftarrow X_t - \eta \nabla_{X_t} \mathcal{L}_t(X_t)$  in Algorithm 1 is taken once per timestep.  $\eta$  is the only hyperparameter in the entire ISAC pipeline.

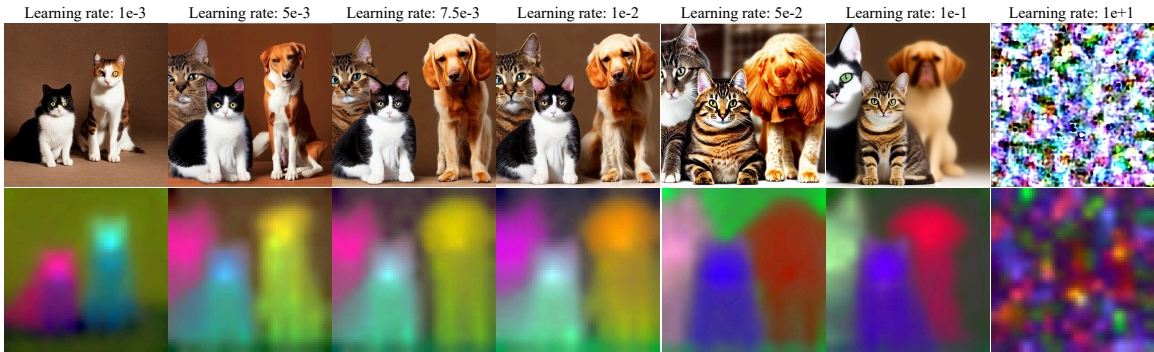


Figure 8: Qualitative comparison of ISAC with various learning rates. For all cases, we provide "A photo of two cats and a dog" as the input prompt and use SD1.5 [1] as the baseline diffusion model.

**Choice of Clustering Algorithm.** We explored alternative clustering algorithms in Table 4 and Figure 9. While all three (K-means, Spectral Clustering, Gaussian Mixture Model) algorithms exhibit similar performance in terms of both multi-class and multi-instance accuracy, K-means (our choice) is  $\times 3$  to  $\times 16$  faster.

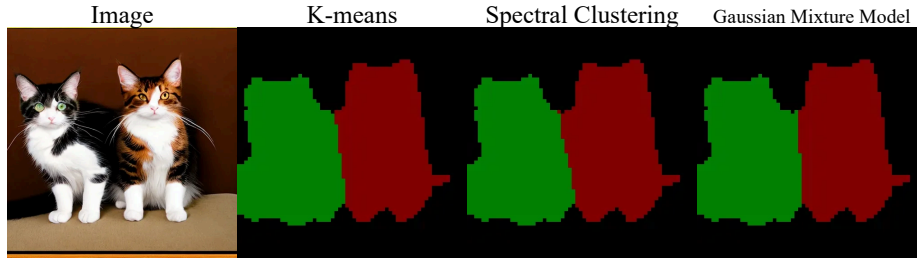


Figure 9: Qualitative comparison of clustering algorithms. The image is generated with the prompt, "a photo of two cats". This figure is an extension of Figure 5.

Table 4: Comparison of clustering algorithms in terms of accuracy (%) and latency (ms). Latency is defined as the execution time for a one-time application of each clustering algorithm to a self-attention map. This table can be seen as an extension of Table 2.

Clustering Algorithm	Multi-class Accuracy ( $\uparrow$ )	Multi-Instance Accuracy ( $\uparrow$ )	Latency (ms) ( $\downarrow$ )
<b>K-means Clustering</b>	<b>36%</b>	<b>69%</b>	<b>505</b>
Spectral Clustering	35%	69%	1,630
Gaussian Mixture Model	36%	69%	8,313

**Attention Accumulation.** We accumulate self- and cross-attention maps with all spatial resolutions for each denoising step. Then, we apply **min-max** normalization to the accumulated maps as shown in Figure 10. For fair comparisons, we use the same attention accumulation scheme for all baseline methods. Details on attention maps and accumulation are given in Section 3.

## B.2 Baseline Implementation Details

**Why the Base Diffusion Model for Baseline Methods is Restricted to SD1.5 in Table 1.** The use of the **softmax** normalization technique in baseline methods (Attend-and-Excite [9], InitNO [11], and TEBOpt [8]) restricts our baseline comparisons to Stable Diffusion v1.5 (SD1.5) [1], as this technique is not directly applicable to other diffusion models. The **softmax** normalization operates by applying the **softmax** function to the cross-attention maps along the token dimension, excluding the **SOT** token at index 0. This sharpens the attention, emphasizing foreground objects while suppressing background noise. The formulation is given by:

$$CA_t^{\text{softmax}} = \text{softmax}(\tau \cdot CA_t[1 :]). \quad (13)$$

Following the baseline implementation, we set  $\tau = 100$  for SD1.5 [1]. SD1.4 and SD2.1 models [1] that share the same architecture as SD1.5 are also tested with the same temperature values in Appendix F.

We found that the temperature hyperparameter  $\tau$  plays a critical role in performance. A large  $\tau$  produces overly sharp cross-attention maps, causing the model to over-focus on a single token and potentially overlook relevant context. In contrast, a small  $\tau$  results in

overly smooth attention maps, which can dilute the focus on foreground objects. As shown in Figure 10, directly applying the temperature value from SD1.5 [1] to SDXL [2] or SD3.5-M [3] leads to undesirable behaviors. For example, in SDXL, a non-instance token such as "of" becomes the most attended token, while in SD3.5-M, the signal is overly diffused after the `softmax` normalization.

This sensitivity to  $\tau$ , along with the lack of official implementations for SDXL [2] and SD3.5-M [3], limits the applicability of baseline methods (Attend-and-Excite, InitNO, TEBOpt) beyond SD1.5 [1].

**Min-max Normalization in ISAC.** In contrast, ISAC requires no temperature tuning. Instead, it adopts a simple element-wise `min-max` normalization to rescale attention maps:

$$CA_t^{\text{minmax}} = \frac{CA_t - \min(CA_t)}{\max(CA_t) - \min(CA_t)}. \quad (14)$$

As illustrated in Figure 10, while `min-max` normalization may retain some background noise, it preserves object-relevant signals more reliably across models. This modification was essential for extending our method to other architectures such as SDXL [2], SD3.5-M [3], and PixArt- $\alpha$  [4]. However, since it is a relatively minor adjustment, we discuss it in the appendix rather than in the main text.

### B.3 Our Benchmark: Multi-Class and Multi-Instance Accuracy

Inspired by the MultiGen benchmark [30], we evaluate ISAC’s ability to generate (1) multiple instances of different classes (multi-class accuracy) and (2) multiple instances of the same class (multi-instance accuracy). Notably, our multi-class evaluation is designed to be more challenging than the original MultiGen setup.

From our observations in Figure 11, text-to-image diffusion models tend to struggle more when generating multiple intra-category instances (e.g., dog and cat) compared to inter-category instances (e.g., animal and vehicle). Based on this insight, our multi-class benchmark emphasizes scenarios where all classes are sampled from the same semantic category.

To facilitate quantitative evaluation, we use a subset of countable object classes from the 80 COCO categories<sup>1</sup> [27], grouped into four higher-level categories: animals, vehicles, sports, and food. The full list of classes and their categorical assignments is provided in Table 5.

We excluded certain COCO classes from our evaluation for the following reasons: The person class was removed due to the difficulty of instance differentiation caused by high variability in pose and posture. We also excluded small or background-like objects such as fork, spoon, knife, keyboard, remote, and toothbrush, which are challenging to detect reliably. In addition, we omitted scene or ambiguous objects like tv, book, clock, vase, bed, and couch, where instance boundaries are often unclear. Finally, we removed objects such as bench, bowl, chair, and dining table, where duplication or spatial overlap lack meaningful semantic distinction.

---

1. Most detection models are trained on COCO classes, so we focus our evaluation on COCO, where the pretrained models are most reliable, rather than experimenting with new classes from datasets like ADE. In practice, benchmarks such as TokenCompose have shown minimal differences in performance trends between COCO and ADE.

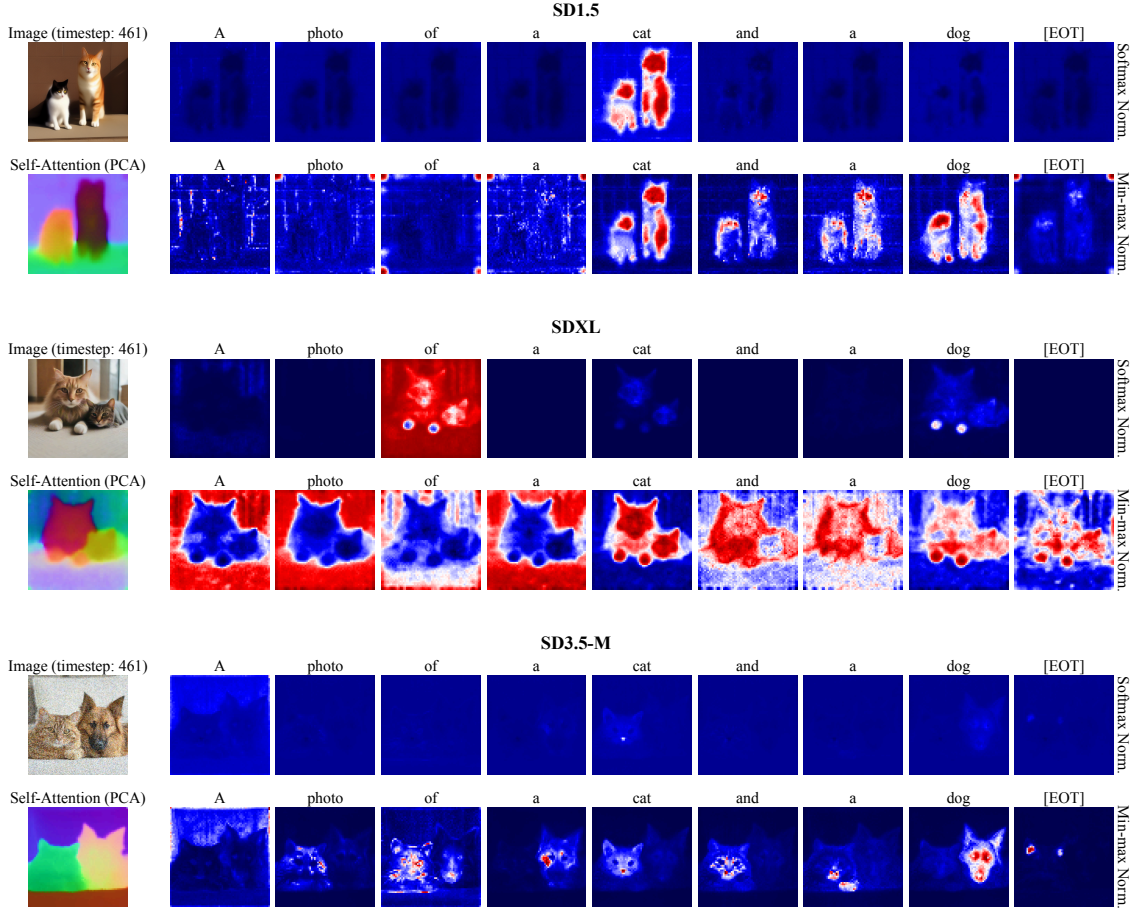


Figure 10: Comparison of cross attention maps after applying softmax and min-max normalization on SD1.5 [1], SDXL [2], SD3.5-M [3]. Here, we used a fixed temperature hyperparameter  $\tau = 100$  across all models.

**Multi-class Accuracy.** For each evaluation, we randomly sample  $k$  classes ( $2 \leq k \leq 5$ ) from a single category and compose a prompt in the form: “A photo of a [class A], a [class B], ..., and a [class E].” For example, when sampling from the animal category, the prompt could be: “A photo of a dog, a cat, a horse, a cow, and a sheep.” The image is then generated using a text-to-image diffusion model conditioned on this prompt.

**Multi-instance Accuracy.** In this setup, we randomly sample a single class  $A$  and specify the number of instances  $n$  ( $2 \leq n \leq 5$ ) to generate. The corresponding prompt is structured as: “A photo of [n] [class A]s.” For instance, if the selected class is “cat” and  $n = 5$ , the prompt would be: “A photo of five cats.” The model is then evaluated on its ability to correctly generate the specified number of instances of the given class.

**Evaluation via Ensemble.** To evaluate the accuracy, we use an ensemble of three state-of-the-art detection models to reduce single detector errors (open-vocabulary detectors—Grounding DINO [19] and YOLOE [29] & closed-vocabulary detector trained on COCO [27]—YOLOv12 [28]). Given a generated image, each model detects the instances in the



(a) *A photo of a cat and a bicycle*



(b) *A photo of a cat and a dog*



Figure 11: Inter-category and intra-category instance generation with 10 random seeds using SDXL [2]. (a) Inter-category instance generation, (b) Intra-category instance generation. We can see that both instances appear in inter-category images with some quality loss (8/10), however, only 3/10 can correctly generate each instance in intra-category images.

Table 5: Countable classes from COCO [27] dataset used in the evaluation.

Category	Classes
Animal	(9 classes) cat, dog, horse, sheep, cow, elephant, bear, zebra, giraffe
Vehicle	(8 classes) bicycle, car, motorcycle, airplane, bus, train, truck, boat
Sports	(10 classes) skateboard, snowboard, skis, sports ball, baseball bat, baseball glove, tennis racket, surfboard, kite, frisbee
Food	(10 classes) banana, apple, sandwich, orange, broccoli, carrot, hot dog, pizza, donut, cake

image. We only leave the detected instances where each instance is captured by any two detectors. The accuracy is then calculated as the ratio of the number of correctly detected instances to the total number of instances. For example, if “cat” and “dog” are detected in the image from the text prompt “A photo of a cat, a dog, a horse, a cow and a sheep”, then the accuracy is calculated as  $2/5 = 40\%$  for multi-class accuracy. For multi-instance accuracy, if 3 instances of “cat” are detected in the image from the text prompt “A photo of five cats”, then the accuracy is calculated as  $3/5 = 60\%$ .

The choice of text prompts and the number of images to be generated are determined as follows. For **multi-class evaluation**, we can achieve all possible combinations of classes to build the text prompts. The number of combinations for each category is shown in Table 6. We randomly sample 20% of the combinations for each category and generate 10 images for each text prompt. For example, in #5-class evaluation, we randomly sample 25 combinations for animal category, 11 combinations for vehicle category, 50 combinations for sports and food categories respectively. In total, we generate 10 images for each of the 136 ( $= 25 + 11 + 50 + 50$ ) text prompts. For **multi-instance evaluation**, we use each class in the category to build a single text prompt. Therefore, we have 9 text prompts for animal category, 8 text prompts for vehicle category, and 10 text prompts for sports and food categories respectively. We generate 10 images for each text prompt. In total, we generate 10 images for each of the 37 ( $= 9 + 8 + 10 + 10$ ) text prompts.

Table 6: Possible combinations of countable classes for multi-class evaluation.

Category	#2	#3	#4	#5
Animal (9 classes)	36	84	126	126
Vehicle (8 classes)	28	56	70	56
Sports (10 classes)	45	120	210	252
Food (10 classes)	45	120	210	252
Total	154	380	616	686

## Appendix C. Broader Related Work Comparisons

To improve the generation of multi-instance images, many training-free methods have been proposed. However, focusing on semantic-level guidance [7–12, 14, 22, 31] is not sufficient to control the instance formation. To overcome this limitation with spatial information, some methods introduce additional instance annotations such as bounding box [32–40] or exploit external models’ prior [18]. In spite of these strong supervision over instances, they still fail to form correct instance structures since they overlooked the importance of forming instance structure in early diffusion steps.

In contrast to these methods, our proposed ISAC focus on instance formation in early diffusion steps. We achieve this by utilizing a hierarchical, tree-structured prompt mechanism that first determines the instance count and then adds semantic information. Since instance counts are easily parsed from text prompts, it adds minimal overhead to prompting compared to other methods that require additional annotations or external models. Table 7 summarizes the differences between ISAC and other methods.

Table 7: Setup comparisons of prior works with ISAC.

Properties	S-CFG [22]	MCR [31]	Box Layout-Guided Methods [32–40]	CG [18]	ISAC (Ours)
requires set of class tokens	✗	✓	✓	✓	✓
requires weak instance supervision (instance counts)	✗	✗	✓	✓	✓
requires strong instance supervision	✗	✗	✓ (bounding box)	✓ (external model)	✗
control instance formation with spatial information?	✗	✗	✓	✓	✓
instance first approach?	✗	✗	✗	✗	✓

**Semantic-aware classifier-free guidance** (S-CFG) [22] points out the spatial inconsistency of the global guidance method, Classifier-free guidance (CFG) [41], and proposes a semantic region-level guidance method leveraging self- and cross-attention maps. However,

Table 8: Quantitative comparisons of ISAC with external model-aided methods. **Bold** indicates the best performance, underline indicates the second best performance.

Method	Use Supervision? (weak/strong)		Multi-Instance Accuracy ( $\uparrow$ )					Latency ( $\downarrow$ )	VRAM ( $\downarrow$ )
	Instance Counts	External Model	#2	#3	#4	#5	Average		
SD1.4 [1]	<b>✗</b>	<b>✗</b>	94%	74%	28%	22%	55%	<b>8s</b>	<b>4.9GB</b>
+ Counting Guidance [18]	<b>✓</b>	<b>✓</b> ( RCC [43] )	79%	67%	32%	19%	49%	<u>14s</u>	17.5GB
+ <b>ISAC (Ours)</b>	<b>✓</b>	<b>✗</b>	<b>100%</b>	<b>90%</b>	<b>51%</b>	<b>40%</b>	<b>70%</b>	21s	<u>9.7GB</u>

S-CFG still lacks the ability to control the overall instance layout, as it only focuses on semantic-level guidance.

**Multi-Concept Resampling**, where we abbreviate it to MCR, proposed by [31] is a method that mixing the noise predictions of single class with the noise predictions of multiple classes. It is aimed to preserve the semantic information of the single instance while generating multiple classes. However, lack of considering the spatial information of the instance, MCR is not able to control the instance formation.

Therefore, controlling the instance formation requires understanding on spatial positioning of instances. Some methods [32–40] utilize **bounding box layout** to provide where the instances should be placed. However, these methods still struggle with overlapping instances [42]. Semantic driven guidance, which is equivalent to separating class appearances with cross-attention maps, is performed on incomplete instance formation with vague boundaries. Therefore, these methods often merge adjacent instance formations into a single, leading to a missing instance.

Another approach is to leverage pretrained vision model to aid the instance formation. **Counting Guidance** [18], where we abbreviate it to CG, proposes a classifier guidance method that leverages the pretrained vision model to aid the instance formation. Specifically, inspired by the Universal Guidance [17], CG applies the counting network [43] (trained to count the number of instances in an image) to intermediate images denoised with Tweedie’s formula [44]. Using the prediction of the counting network, CG then guides the diffusion process to generate the desired number of instances. However, blurry and semantically poor intermediate images in early diffusion steps make the pretrained vision model less effective. As illustrated in Figure 12, it is hard to tell what each instance is in the intermediate images and the state-of-the-art vision models, such as Grounding DINO [19] and YOLOE [29], fail to provide accurate predictions. On the other hand, vision models are trained on clean, semantically rich images. This domain mismatch makes predictions of pretrained vision models in early diffusion steps less effective. Table 8 supports this observation, showing that the counting guidance [18] is less effective than ISAC in terms of instance formation.

Additionally, while universal guidance [17] propose to apply vision model predictions on tweedie-denoised [44] images, tweedie formula cannot be applied to flow matching [45] based models, such as SD3.5-M [3]. This even hinders the application of the pretrained vision models to flow matching based models.

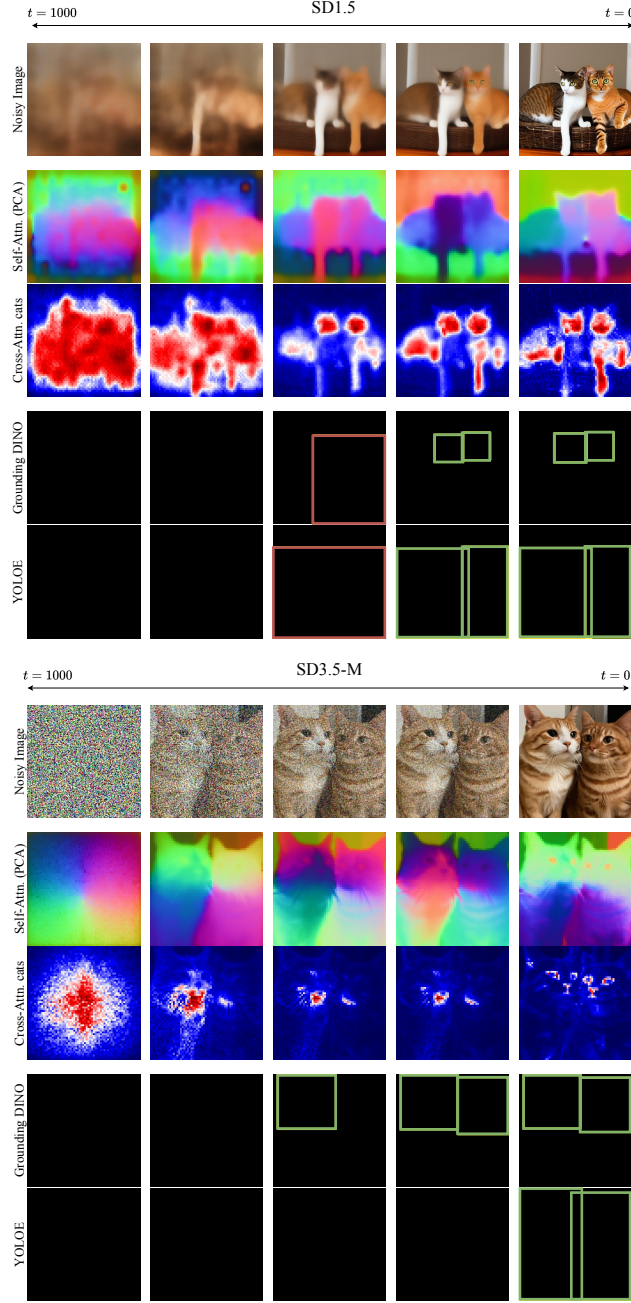


Figure 12: Dynamics of text-to-image diffusion models. For SD1.5 [1], we visualize the tweedie-denoised [44] image as noisy images, then apply detection models on the denoised images following universal guidance [17]. Self-attention maps are visualized by PCA projection of the attention maps. The attention maps are obtained as explained in Appendix B. For each bounding box prediction of the detection model, if it is correct, we color it in green, and if it is incorrect, we color it in red.



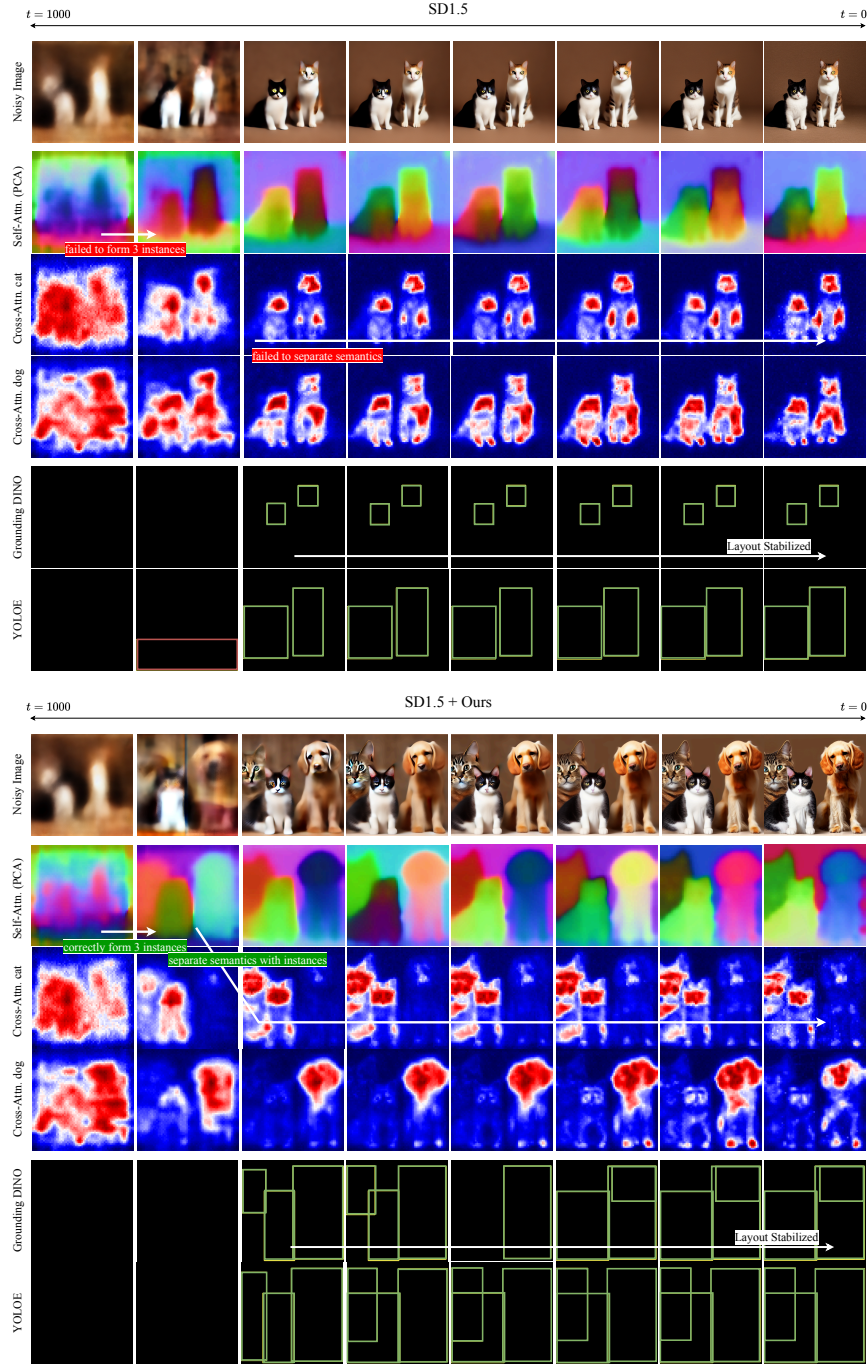


Figure 13: Qualitative comparisons of evolving dynamics of SD1.5 [1] with and without ISAC control. We visualize the tweedie-denoised [44] image as noisy images, then apply detection models on the denoised images. Self-attention maps are visualized by PCA projection of the attention maps. The attention maps are obtained as explained in Appendix B. For each bounding box prediction of the detection model, if it is correct, we color it in green, and if it is incorrect, we color it in red.

## Appendix D. Dynamics Analysis of Diffusion Models

### D.1 Self-Attention Maps Implies Instance Formation

In Figure 12, we visualize the evolution of denoising process. It contains noisy images, PCA visualization of self-attention maps, cross-attention maps on a token “cats” and detection models’ predictions on each noisy image. From the evolution of noisy images, we can see that instance structures are formed in the early denoising steps (until 3rd column), and the instance structures are preserved in the later denoising steps. Self-attention maps follow the same trend, where the attention maps are more focused on the instance structures in the early denoising steps. This shows that self-attention maps are able to capture the instance formation process of diffusion models. Predictions of detection models also share the same turning point that after the instance structures are formed and each instance become semantically identifiable, the predictions become correct. Semantically poor images in early denoising steps, where instance formation is actively done, make the use of pretrained vision models to aid instance formation process less effective.

### D.2 Visualization of Dynamics Aligned Attention Control

Figure 13 shows how ISAC’s instance forming first approach enhances multi-instance generation. ISAC first applies guidance to the self-attention maps, which helps to form correct number of instances in the early denoising steps. Then, leveraging the stand out instance structures, ISAC applies guidance to the instance-aware cross-attention maps to encourage each class appearance to be separated into its dedicated instance structure. Without instance control, however, SD1.5 [1] not only fail to form correct number of instances, but also class semantics spread across the instance structures.

It is worth note that the instance forming guidance should be applied in the early denoising steps, otherwise the instance structures are already formed and the guidance will not be effective. The prediction results of Grounding DINO [19] and YOLOE [29] also support that their predictions are only effective after each instance in noisy image contains distinguishable semantic information. This mismatch highlights ISAC’s advantage of instance forming first approach.

## Appendix E. ISAC Extension with Fine-tuned Models

We extend ISAC to fine-tuning based methods—TokenCompose [30] and IterComp [46], which amplify their spatial understanding using external models. TokenCompose [30] first generate an image with a base diffusion model. Next, obtain the ground-truth segmentation maps of the generated image by leveraging Grounded SAM [19, 47]. Then, it trains the model by making cross-attention maps correspond to the segmentation maps, thereby achieving an improvement over multi-class generation. IterComp [46] employs an iterative refinement strategy with model preferences over multiple specialized models. The capabilities of RPG [42] and InstanceDiffusion [48], which leverage Large Language Model (LLM) and box-layout guided methods, respectively, are infused to improve the spatial understanding of the model.

Table 9 shows the results of ISAC extension to these models. Even combined on the top of the fine-tuned models, ISAC shows a significant improvement over the baselines. As a

Table 9: Extension of ISAC to fine-tuned models.

Method	Multi-Class Accuracy ( $\uparrow$ )					Multi-Instance Accuracy ( $\uparrow$ )					Latency ( $\downarrow$ )	VRAM ( $\downarrow$ )
	#2	#3	#4	#5	Average	#2	#3	#4	#5	Average		
TokenCompose <sub>SD1.4</sub> [30]	27%	4%	1%	0%	8%	77%	65%	41%	13%	49%	<b>12s</b>	<b>8.5GB</b>
<b>+ ISAC (Ours)</b>	<b>62%</b>	<b>36%</b>	<b>28%</b>	<b>17%</b>	<b>36%</b>	<b>84%</b>	<b>80%</b>	<b>60%</b>	<b>30%</b>	<b>63%</b>	33s	17.9GB
IterComp <sub>SDXL</sub> [46]	11%	5%	4%	0%	5%	95%	73%	64%	37%	67%	<b>49s</b>	<b>11.8GB</b>
<b>+ ISAC (Ours)</b>	<b>46%</b>	<b>28%</b>	<b>26%</b>	<b>21%</b>	<b>30%</b>	<b>99%</b>	<b>93%</b>	<b>85%</b>	<b>55%</b>	<b>83%</b>	100s	29.9GB

minor note, TokenCompose [30] uses `float32` data type for model weights. It causes both latency and VRAM usage to be increased by 2x compared to the original results of SD1.4 [1].

## Appendix F. Additional Quantitative Results

We provide additional quantitative results in Table 10. The results are obtained by applying ISAC to various models, including SD1.4, SD1.5, SD2.1 [1], SDXL [2], SD3.5-M [3], PixArt- $\alpha$  [4], and PixArt- $\Sigma$  [49].

Our evaluation methodology leverages object detection models such as Grounding DINO [19], which aligns closely with the MultiGen benchmark [30]—an official benchmark for assessing multi-instance generation performance. Due to the high variability and noise observed in some public open-vocabulary detection settings (e.g., UniDet [50], Grounding DINO [19]), we refrain from including these results in the main paper. Nonetheless, we provide them in the appendix for reference.

**Public Benchmarks.** For completeness and to support broader understanding, we additionally report results on public benchmarks such as T2I-CompBench++ (Numeracy) [51] in Table 11. The T2I-CompBench++ Numeracy benchmark evaluates not only multi-instance generation but also more complex multi-(class+instance) scenarios. The first 90 lines (e.g., “two cars stuck on the road”) focus on multi-instance generation, while the remaining lines (91–300) include more challenging multi-class and multi-instance compositions. Interestingly, ISAC on SD1.5 [1] surpasses SDXL [2] despite having only one-third the number of parameters.

## Appendix G. Additional Qualitative Results

**Generality Beyond Animals and Simple Prompts.** Readers may be interested in whether our method is effective for more complex sentence structures and a wider variety of object classes. We provide qualitative results that include prompts with diverse object classes and relational structures in Figure 14. All prompts are taken from T2I-CompBench++ (Numeracy) [51] benchmark.

These results highlight the generality of ISAC to a wide range of object classes and complex prompts. Aligning with the quantitative gains across a wide range of classes and text prompt complexity, our method consistently improves the quality of generated images, demonstrating its robustness and versatility.

**Robust Multi-instance Generation Across Seeds.** We provide qualitative results when generating 5 images with a fixed prompt, “*three cats*”, on SD1.5 [1] and SD3.5-M [3]. When the baseline output already contains the correct number of instances, ISAC minimally

Table 10: Full quantitative results.

Method	Multi-Class Accuracy ( $\uparrow$ )					Multi-Instance Accuracy ( $\uparrow$ )					Latency ( $\downarrow$ )	VRAM ( $\downarrow$ )
	#2	#3	#4	#5	Average	#2	#3	#4	#5	Average		
SD1.4 [1]	30%	2%	1%	0%	8%	94%	74%	28%	22%	55%	<b>8s</b>	<b>4.9GB</b>
+ A&E [9]	50%	9%	8%	2%	17%	97%	79%	26%	23%	56%	17s	9.2GB
+ SynGen [10]	54%	11%	6%	2%	18%	90%	69%	25%	19%	51%	19s	9.3GB
+ InitNO [11]	58%	10%	7%	4%	20%	94%	79%	31%	20%	56%	20s	9.6GB
+ TEBOpt [8]	55%	13%	8%	2%	19%	91%	73%	31%	20%	54%	17s	9.3GB
<b>+ ISAC (Ours)</b>	<b>66%</b>	<b>34%</b>	<b>29%</b>	<b>16%</b>	<b>36%</b>	<b>100%</b>	<b>90%</b>	<b>51%</b>	<b>40%</b>	<b>70%</b>	21s	9.7GB
SD1.5 [1]	28%	2%	1%	0%	8%	88%	65%	36%	26%	54%	<b>12s</b>	<b>4.4GB</b>
+ A&E [9]	48%	10%	5%	2%	16%	91%	68%	34%	24%	54%	24s	9.1GB
+ SynGen [10]	50%	9%	4%	2%	16%	84%	61%	38%	22%	51%	27s	9.2GB
+ InitNO [11]	55%	12%	7%	5%	20%	90%	68%	40%	29%	57%	29s	9.5GB
+ TEBOpt [8]	52%	11%	8%	3%	18%	87%	65%	36%	27%	54%	25s	9.2GB
<b>+ ISAC (Ours)</b>	<b>65%</b>	<b>31%</b>	<b>29%</b>	<b>18%</b>	<b>36%</b>	<b>95%</b>	<b>82%</b>	<b>56%</b>	<b>44%</b>	<b>69%</b>	30s	9.6GB
SD2.1 [1]	31%	6%	3%	0%	10%	91%	74%	41%	28%	58%	<b>13s</b>	<b>4.8GB</b>
+ A&E [9]	53%	12%	4%	1%	18%	94%	79%	39%	29%	60%	26s	9.3GB
+ SynGen [10]	55%	10%	7%	3%	19%	87%	69%	38%	25%	55%	29s	9.4GB
+ InitNO [11]	59%	13%	11%	5%	22%	91%	79%	44%	26%	60%	31s	9.7GB
+ TEBOpt [8]	56%	14%	7%	6%	21%	88%	75%	44%	27%	58%	27s	9.4GB
<b>+ ISAC (Ours)</b>	<b>67%</b>	<b>35%</b>	<b>34%</b>	<b>20%</b>	<b>39%</b>	<b>98%</b>	<b>88%</b>	<b>64%</b>	<b>42%</b>	<b>73%</b>	32s	9.8GB
SDXL [2]	20%	4%	3%	0%	7%	90%	71%	49%	32%	61%	<b>48s</b>	<b>12.8GB</b>
<b>+ ISAC (Ours)</b>	<b>57%</b>	<b>32%</b>	<b>29%</b>	<b>17%</b>	<b>34%</b>	<b>96%</b>	<b>89%</b>	<b>71%</b>	<b>47%</b>	<b>76%</b>	101s	29.8GB
PixArt- $\alpha$ [4]	27%	3%	1%	0%	8%	99%	93%	33%	15%	60%	<b>17s</b>	<b>19.9GB</b>
<b>+ ISAC (Ours)</b>	<b>63%</b>	<b>30%</b>	<b>29%</b>	<b>21%</b>	<b>36%</b>	<b>100%</b>	<b>100%</b>	<b>56%</b>	<b>31%</b>	<b>72%</b>	40s	53.7GB
PixArt- $\Sigma$ [49]	39%	8%	0%	0%	12%	98%	98%	30%	16%	60%	<b>18s</b>	<b>19.9GB</b>
<b>+ ISAC (Ours)</b>	<b>78%</b>	<b>39%</b>	<b>31%</b>	<b>20%</b>	<b>42%</b>	<b>100%</b>	<b>100%</b>	<b>48%</b>	<b>31%</b>	<b>70%</b>	41s	53.8GB
SD3.5-M [3]	62%	23%	12%	3%	25%	84%	71%	51%	51%	64%	<b>40s</b>	<b>22.9GB</b>
<b>+ ISAC (Ours)</b>	<b>98%</b>	<b>51%</b>	<b>40%</b>	<b>20%</b>	<b>52%</b>	<b>98%</b>	<b>91%</b>	<b>72%</b>	<b>69%</b>	<b>83%</b>	140s	74.8GB

Table 11: Additional quantitative results on T2I-CompBench++ (Numeracy) [51] benchmark. **Bold** indicates the best performance, underline indicates the second best performance.

Method	# Parameters	T2I-CompBench++ (Numeracy)
SD1.5 [1]	0.8B	46.5%
<b>+ ISAC (Ours)</b>	0.8B	<u>54.3%</u>
SDXL [2]	2.6B	50.7%
<b>+ ISAC (Ours)</b>	2.6B	<b>63.4%</b>

alters the result. However, when the baseline produces too few or too many instances, ISAC effectively corrects the output (see Figures 15a and 15b). These results show that ISAC reliably helps correct instance counts across diverse seeds for a fixed prompt, while leaving correct samples mostly unchanged.

These results highlight ISAC’s ability to consistently assist instance generation across diverse seeds for a fixed prompt—correcting incorrect instance counts while leaving already correct samples largely unchanged—demonstrating that the qualitative improvements align



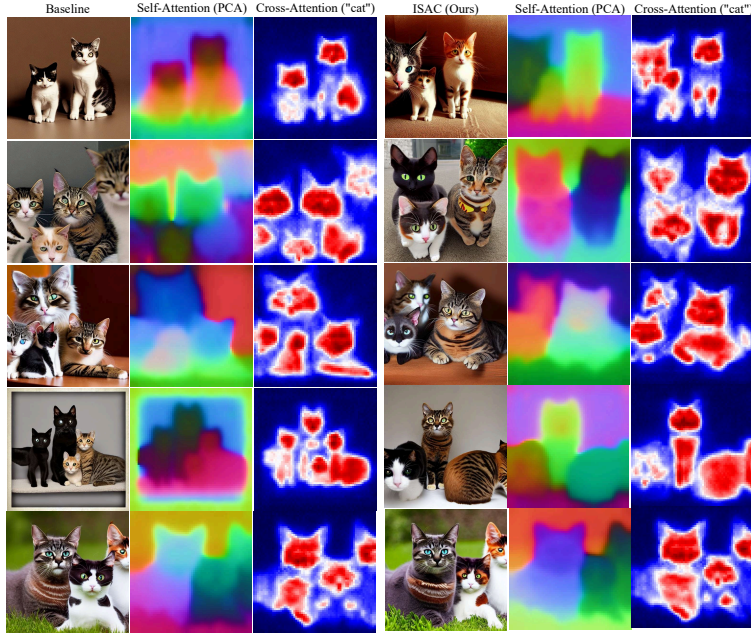
well with the gains observed in quantitative metrics across a wide range of classes beyond the animal examples discussed in the main text.

## **Appendix H. Future Work**

**Extension to Distilled Diffusion Models.** The timestep-wise instance-to-semantic dynamics observed in standard diffusion models appear to be compressed into a layer-wise instance-to-semantic dynamics in SDXL-Turbo [52] (see Figure 16). This observation suggests that our method, ISAC, could potentially be extended to improve multi-class/multi-instance generation in distilled models (e.g., consistency models) as well.



Figure 14: Qualitative results beyond animals and simple prompts. SD1.5 [1] with our method shows consistent success across variety of object classes. All prompts are taken from T2I-CompBench++ (Numeracy) [51] benchmark. 10 different seeds are used for each prompt to synthesize images.



(a) Result from Stable Diffusion v1.5 [1].



(b) Result from Stable Diffusion v3.5-M [3].

Figure 15: Qualitative results across multiple seeds for the prompt *"three cats"*, which involves multiple instances of the same class. Our method (right) consistently generates images with the correct instance count, sharper object boundaries, and improved separation compared to the baseline (left).



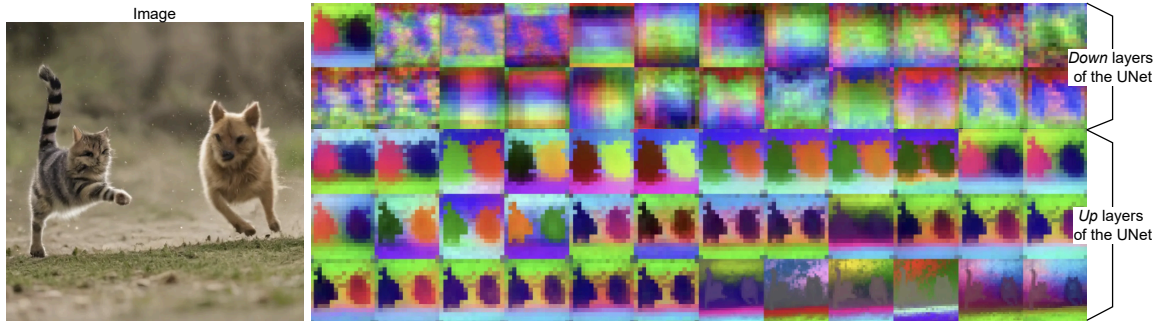


Figure 16: PCA visualizations of self-attention maps in the *down* and *up* layers of the UNet in SDXL-Turbo [52]. The timestep-wise instance-to-semantic dynamics observed in standard diffusion models appear to be compressed into a layer-wise instance-to-semantic dynamics in distilled models.

## References

- [1] R. Rombach, A. Blattmann, D. Lorenz, P. Esser, and B. Ommer, “High-resolution image synthesis with latent diffusion models,” in *Proceedings of the IEEE/CVF conference on computer vision and pattern recognition*, pp. 10684–10695, 2022.
- [2] D. Podell, Z. English, K. Lacey, A. Blattmann, T. Dockhorn, J. Müller, J. Penna, and R. Rombach, “Sdxl: Improving latent diffusion models for high-resolution image synthesis,” *arXiv preprint arXiv:2307.01952*, 2023.
- [3] P. Esser, S. Kulal, A. Blattmann, R. Entezari, J. Müller, H. Saini, Y. Levi, D. Lorenz, A. Sauer, F. Boesel, *et al.*, “Scaling rectified flow transformers for high-resolution image synthesis,” in *Forty-first international conference on machine learning*, 2024.
- [4] J. Chen, J. Yu, C. Ge, L. Yao, E. Xie, Y. Wu, Z. Wang, J. Kwok, P. Luo, H. Lu, and Z. Li, “Pixart- $\alpha$ : Fast training of diffusion transformer for photorealistic text-to-image synthesis,” 2023.
- [5] B. F. Labs, “Flux.” <https://github.com/black-forest-labs/flux>, 2024.
- [6] A. Hertz, R. Mokady, J. Tenenbaum, K. Aberman, Y. Pritch, and D. Cohen-Or, “Prompt-to-prompt image editing with cross attention control,” *arXiv preprint arXiv:2208.01626*, 2022.
- [7] W. Feng, X. He, T.-J. Fu, V. Jampani, A. R. Akula, P. Narayana, S. Basu, X. E. Wang, and W. Y. Wang, “Training-free structured diffusion guidance for compositional text-to-image synthesis,” in *The Eleventh International Conference on Learning Representations*, 2023.
- [8] C.-Y. Chen, C. Tseng, L.-W. Tsao, and H.-H. Shuai, “A cat is a cat (not a dog!): Unraveling information mix-ups in text-to-image encoders through causal analysis and embedding optimization,” *Advances in Neural Information Processing Systems*, 2024.
- [9] H. Chefer, Y. Alaluf, Y. Vinker, L. Wolf, and D. Cohen-Or, “Attend-and-excite: Attention-based semantic guidance for text-to-image diffusion models,” 2023.
- [10] R. Rassin, E. Hirsch, D. Glickman, S. Ravfogel, Y. Goldberg, and G. Chechik, “Linguistic binding in diffusion models: Enhancing attribute correspondence through attention map alignment,” *Advances in Neural Information Processing Systems*, vol. 36, 2024.
- [11] X. Guo, J. Liu, M. Cui, J. Li, H. Yang, and D. Huang, “Initno: Boosting text-to-image diffusion models via initial noise optimization,” in *CVPR*, 2024.
- [12] T. Hu, L. Li, J. van de Weijer, H. Gao, F. Shahbaz Khan, J. Yang, M.-M. Cheng, K. Wang, and Y. Wang, “Token merging for training-free semantic binding in text-to-image synthesis,” *Advances in Neural Information Processing Systems*, vol. 37, pp. 137646–137672, 2024.
- [13] A. M. Izadi, S. M. H. Hosseini, S. V. Tabar, A. Abdollahi, A. Saghaian, and M. S. Baghshah, “Fine-grained alignment and noise refinement for compositional text-to-image generation,” *arXiv preprint arXiv:2503.06506*, 2025.
- [14] T. H. S. Meral, E. Simsar, F. Tombari, and P. Yanardag, “Conform: Contrast is all you need for high-fidelity text-to-image diffusion models,” in *Proceedings of the IEEE/CVF Conference on Computer Vision and Pattern Recognition*, pp. 9005–9014, 2024.
- [15] A. Radford, J. W. Kim, C. Hallacy, A. Ramesh, G. Goh, S. Agarwal, G. Sastry, A. Askell, P. Mishkin, J. Clark, *et al.*, “Learning transferable visual models from natural language supervision,” in *International conference on machine learning*, pp. 8748–8763, PmLR, 2021.

- [16] S. Jo, Z. Lee, W. Lee, and K. Kim, “Diffegg: Diffusion-driven edge generation as a pixel-annotation-free alternative for instance annotation,” 2025.
- [17] A. Bansal, H.-M. Chu, A. Schwarzschild, S. Sengupta, M. Goldblum, J. Geiping, and T. Goldstein, “Universal guidance for diffusion models,” in *Proceedings of the IEEE/CVF Conference on Computer Vision and Pattern Recognition*, pp. 843–852, 2023.
- [18] W. Kang, K. Galim, H. I. Koo, and N. I. Cho, “Counting guidance for high fidelity text-to-image synthesis,” in *2025 IEEE/CVF Winter Conference on Applications of Computer Vision (WACV)*, pp. 899–908, IEEE, 2025.
- [19] S. Liu, Z. Zeng, T. Ren, F. Li, H. Zhang, J. Yang, Q. Jiang, C. Li, J. Yang, H. Su, *et al.*, “Grounding dino: Marrying dino with grounded pre-training for open-set object detection,” in *European Conference on Computer Vision*, pp. 38–55, Springer, 2024.
- [20] H. Lee, H. Lee, S. Gye, and J. Kim, “Beta sampling is all you need: Efficient image generation strategy for diffusion models using stepwise spectral analysis,” in *2025 IEEE/CVF Winter Conference on Applications of Computer Vision (WACV)*, pp. 4215–4224, IEEE, 2025.
- [21] J. Ho, A. Jain, and P. Abbeel, “Denoising diffusion probabilistic models,” *Advances in neural information processing systems*, vol. 33, pp. 6840–6851, 2020.
- [22] D. Shen, G. Song, Z. Xue, F.-Y. Wang, and Y. Liu, “Rethinking the spatial inconsistency in classifier-free diffusion guidance,” in *Proceedings of the IEEE/CVF Conference on Computer Vision and Pattern Recognition*, pp. 9370–9379, 2024.
- [23] J. Wang, X. Li, J. Zhang, Q. Xu, Q. Zhou, Q. Yu, L. Sheng, and D. Xu, “Diffusion model is secretly a training-free open vocabulary semantic segmenter,” *IEEE Transactions on Image Processing*, 2025.
- [24] T. N. Kipf and M. Welling, “Semi-supervised classification with graph convolutional networks,” *arXiv preprint arXiv:1609.02907*, 2016.
- [25] H. Zhu and P. Koniusz, “Simple spectral graph convolution,” in *International conference on learning representations*, 2021.
- [26] L. Binyamin, Y. Tewel, H. Segev, E. Hirsch, R. Rassin, and G. Chechik, “Make it count: Text-to-image generation with an accurate number of objects,” *arXiv preprint arXiv:2406.10210*, 2024.
- [27] T.-Y. Lin, M. Maire, S. Belongie, J. Hays, P. Perona, D. Ramanan, P. Dollár, and C. L. Zitnick, “Microsoft COCO: Common objects in context,” in *ECCV*, pp. 740–755, Springer, 2014.
- [28] Y. Tian, Q. Ye, and D. Doermann, “Yolov12: Attention-centric real-time object detectors,” *arXiv preprint arXiv:2502.12524*, 2025.
- [29] A. Wang, L. Liu, H. Chen, Z. Lin, J. Han, and G. Ding, “Yoloe: Real-time seeing anything,” 2025.
- [30] Z. Wang, Z. Sha, Z. Ding, Y. Wang, and Z. Tu, “Tokencompose: Text-to-image diffusion with token-level supervision,” in *Proceedings of the IEEE/CVF Conference on Computer Vision and Pattern Recognition (CVPR)*, pp. 8553–8564, June 2024.
- [31] G. Kwon and J. C. Ye, “Tweediemix: Improving multi-concept fusion for diffusion-based image/video generation,” in <https://arxiv.org/abs/2410.05591>, 2024.

- [32] O. Bar-Tal, L. Yariv, Y. Lipman, and T. Dekel, “Multidiffusion: Fusing diffusion paths for controlled image generation,” *arXiv preprint arXiv:2302.08113*, 2023.
- [33] T. Shirakawa and S. Uchida, “Noisecollage: A layout-aware text-to-image diffusion model based on noise cropping and merging,” in *Proceedings of the IEEE/CVF Conference on Computer Vision and Pattern Recognition*, 2024.
- [34] J. Xie, Y. Li, Y. Huang, H. Liu, W. Zhang, Y. Zheng, and M. Z. Shou, “Boxdiff: Text-to-image synthesis with training-free box-constrained diffusion,” in *Proceedings of the IEEE/CVF International Conference on Computer Vision (ICCV)*, pp. 7452–7461, 2023.
- [35] M. Chen, I. Laina, and A. Vedaldi, “Training-free layout control with cross-attention guidance,” *arXiv preprint arXiv:2304.03373*, 2023.
- [36] J. Xiao, L. Li, H. Lv, S. Wang, and Q. Huang, “R&b: Region and boundary aware zero-shot grounded text-to-image generation,” 2023.
- [37] O. Dahary, O. Patashnik, K. Aberman, and D. Cohen-Or, “Be yourself: Bounded attention for multi-subject text-to-image generation,” 2024.
- [38] P. Y. Lee, T. Yoon, and M. Sung, “Groundit: Grounding diffusion transformers via noisy patch transplantation,” in *Advances in Neural Information Processing Systems*, 2024.
- [39] L. Lian, B. Li, A. Yala, and T. Darrell, “Llm-grounded diffusion: Enhancing prompt understanding of text-to-image diffusion models with large language models,” *arXiv preprint arXiv:2305.13655*, 2023.
- [40] D. Park, S. Kim, T. Moon, M. Kim, K. Lee, and J. Cho, “Rare-to-frequent: Unlocking compositional generation power of diffusion models on rare concepts with llm guidance,” *The Thirteenth International Conference on Learning Representations*, 2025.
- [41] J. Ho and T. Salimans, “Classifier-free diffusion guidance,” *arXiv preprint arXiv:2207.12598*, 2022.
- [42] L. Yang, Z. Yu, C. Meng, M. Xu, S. Ermon, and B. Cui, “Mastering text-to-image diffusion: Recaptioning, planning, and generating with multimodal llms,” in *International Conference on Machine Learning*, 2024.
- [43] M. Hobley and V. Prisacariu, “Learning to count anything: Reference-less class-agnostic counting with weak supervision,” *arXiv preprint arXiv:2205.10203*, 2022.
- [44] K. Kim and J. C. Ye, “Noise2score: tweedie’s approach to self-supervised image denoising without clean images,” *Advances in Neural Information Processing Systems*, vol. 34, pp. 864–874, 2021.
- [45] Y. Lipman, R. T. Chen, H. Ben-Hamu, M. Nickel, and M. Le, “Flow matching for generative modeling,” *arXiv preprint arXiv:2210.02747*, 2022.
- [46] X. Zhang, L. Yang, G. Li, Y. Cai, J. Xie, Y. Tang, Y. Yang, M. Wang, and B. Cui, “Itercomp: Iterative composition-aware feedback learning from model gallery for text-to-image generation,” *arXiv preprint arXiv:2410.07171*, 2024.
- [47] A. Kirillov, E. Mintun, N. Ravi, H. Mao, C. Rolland, L. Gustafson, T. Xiao, S. Whitehead, A. C. Berg, W.-Y. Lo, *et al.*, “Segment anything,” in *Proceedings of the IEEE/CVF international conference on computer vision*, pp. 4015–4026, 2023.

- [48] X. Wang, T. Darrell, S. S. Rambhatla, R. Girdhar, and I. Misra, “Instancediffusion: Instance-level control for image generation,” 2024.
- [49] J. Chen, C. Ge, E. Xie, Y. Wu, L. Yao, X. Ren, Z. Wang, P. Luo, H. Lu, and Z. Li, “Pixart- $\sigma$ : Weak-to-strong training of diffusion transformer for 4k text-to-image generation,” in *European Conference on Computer Vision*, pp. 74–91, Springer, 2024.
- [50] X. Zhou, V. Koltun, and P. Krähenbühl, “Simple multi-dataset detection,” in *Proceedings of the IEEE/CVF conference on computer vision and pattern recognition*, pp. 7571–7580, 2022.
- [51] K. Huang, C. Duan, K. Sun, E. Xie, Z. Li, and X. Liu, “T2i-compbench++: An enhanced and comprehensive benchmark for compositional text-to-image generation,” *IEEE Transactions on Pattern Analysis and Machine Intelligence*, vol. 47, no. 5, pp. 3563–3579, 2025.
- [52] A. Sauer, D. Lorenz, A. Blattmann, and R. Rombach, “Adversarial diffusion distillation,” in *European Conference on Computer Vision*, pp. 87–103, Springer, 2024.